10

Development of a Broadband and Squint-Free K_u-Band Phased Array Antenna System for Airborne Satellite Communications

David Marpaung[1], Chris Roeloffzen[1], Willem Beeker[2], Bertrand Noharet[3], Jaco Verpoorte[4] and Rens Baggen[5]
[1]*University of Twente,*
[2]*LioniX BV,*
[3]*Acreo AB,*
[4]*National Aerospace Laboratory (NLR),*
[5]*IMST GmbH,*
[1,2,4]*The Netherlands*
[3]*Sweden*
[5]*Germany*

1. Introduction

Novel avionic communication systems are required for various purposes, for example to increase the flight safety and operational integrity as well as to enhance the quality of service to passengers on board. To serve these purposes, a key technology that is essential to be developed is an antenna system that can provide broadband connectivity within aircraft cabins at an affordable price. Currently, in the European Commission (EC) 7th Framework Programme SANDRA project (SANDRA, 2011), a development of such an antenna system is being carried out. The system is an electronically-steered phased-array antenna (PAA) with a low aerodynamic profile. The reception of digital video broadcasting by satellite (DVB-S) signal which is in the frequency range of 10.7-12.75 GHz (K_u-band) is being considered. In order to ensure the quality of service provided to the passengers, the developed antenna should be able to receive the entire DVB-S band at once while complying with the requirements of the DVB-S system (Morello & Mignone, 2006). These requirements, as will be explained later, dictate a broadband antenna system where the beam is squint-free, i.e. no variation of beam pointing direction for all the frequencies in the desired band. Additionally, to track the satellite, the seamless tunability of the beam pointing direction of this antenna is also required. In this work, a concept of optical beamforming (Riza & Thompson, 1997) is implemented to provide a squint-free beam over the entire K_u-band for all the desired pointing directions. The optical beamformer itself consists of continuously tunable optical delay lines that enable seamless tunability of the beam pointing direction.

Although this particular concept of optical beamforming has been well investigated in the past (Meijerink et al., 2010; Zhuang et al., 2007, 2010), its implementation in the actual antenna system is by no means trivial. It requires extensive modelling of the antenna system, development of the system components that operate in the radio frequency (RF)

and/or the optical domains as well as the integration between these components to yield a compact and reliable system. This chapter focuses on these aspects towards the development of a full antenna system.
The remainder of this chapter is organized as follows: in Section 2 the target specifications of the PAA system is discussed. In Section 3, the concept of optical beamforming using optical ring resonators as delay elements is explained. The system modelling and performance analysis is presented in Section 4. In Section 5 the current status of the development of the components in the system is reported. In Section 6 the photonic integration scheme is discussed. The chapter closes with conclusions.

2. Antenna specifications

The intended operation of the PAA system is illustrated in Fig. 1. Antenna tiles (8x8), each consisting of 64 antenna elements (AEs), are arranged to form the total PAA system with a large number of AEs. As mentioned earlier this PAA is thus used to provide airplane passengers with live television service received from a satellite. To ensure proper signal receptions, the PAA should fulfil a set of requirements. The list of target specifications of the PAA is listed in Table 1.

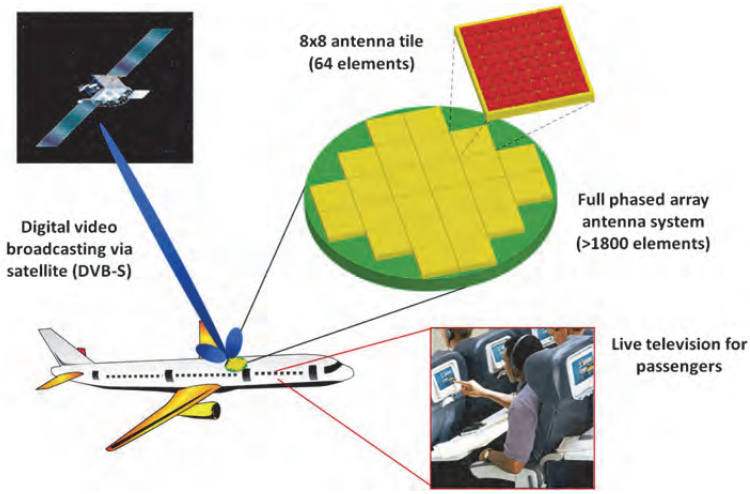

Fig. 1. Illustration of the system considered in this work. In order to provide airplane passengers with live television channels, a phased array antenna system is used for reception. The antenna consists of antenna tiles of 64 elements.

In this PAA, the received K_u-band signal is down-converted to the L-band and is subsequently processed in the beamformer. The beamformer delays and combines the signals from the AEs such that they are synchronized at the beamformer output. The time delay provided by the beamformer should be sufficient to incorporate the intended maximum scanning angle of this PAA system, which in this case is 360° in the azimuth plane and 60° in the elevation angle. Besides the maximum scanning angle, the factors that determine the required maximum time delay are the spacing between the AEs (1.18 cm in this case) and subsequently the size of the antenna. This will be explained further when the design of the beamfomer is discussed in Subsection 5.3.2.

Antenna parameter	Target value
Frequency range	10.7-12.75 GHz (Ku-band)
Frequency range after downconversion	950-3000 MHz (L-band)
Inter-element distance	1.18 cm
Steering type	Electrical, continuous
Beam steering angle	Azimuth: 360^o Elevation: 60^o
Beam tracking accuracy	0.1^o
G/T	12.7 dB/K
Antenna size	Diameter: 60 cm Height: 10 cm
Number of elements	2048
Antenna gain	35 dBi
Polarization	Linear (H/V)

Table 1. The phased array antenna specifications targeted in this work.

The size of the antenna will also determine the antenna gain. Here, the aim is to have an antenna with a diameter of 60 cm, with a gain in the order of 35 dBi. It has been shown that this dictates at least 1800 AEs incorporated in the system (Meijerink et al., 2010). In this work we set the number of AEs to be 2048. Finally, a useful figure of merit for an antenna system is the antenna gain-to-noise temperature (G/T) which is the ratio of the antenna gain and the antenna noise temperature (in Kelvin), expressed in decibels. The G/T target value for the antenna is 12.7 dB/K. This parameter is strongly related to the antenna system architecture and will be discussed in depth in Subsection 4.1, where the system design is described.

3. Optical beamforming

The beamforming network (BFN) is a crucial part of the entire PAA system. In this work, where a broadband, squint-free and seamless beam steering is targeted, the BFN needs to provide continuously tunable time delay. In the past, many have turned to photonic delay lines to provide true time delay (TTD) (i.e. linear phase progression over the frequency) (Riza & Thompson, 1997; Meijerink et al., 2010). This is in contrast to phase shifters that provide a constant phase shift over the frequency, which will induce beam-squint for a broadband signal (Baggen et al., 2011).

Various photonic delay line structures have been proposed as the TTD element, ranging from optical fibers, fiber Bragg gratings, semiconductor optical amplifier (SOA), and integrated photonic filters. Each approach claims to offer advantage either in terms of maximum achievable delay, tunability, size and compactness, cost and/or simplicity in operation (Meijerink et al., 2010).

In the past, we have proposed a photonic BFN with optical ring resonator (ORR) filters serving as the TTD elements (Zhuang et al., 2007) which will be explained in the following subsection.

3.1 Optical ring resonator

When an optical carrier is modulated by an RF signal, propagates through an optical waveguide, and is converted to the electrical domain by an optical detector, the effective time delay to the RF signal is determined by the group delay of this optical waveguide. This group delay can be made tunable by putting an ORR parallel to the waveguide, as illustrated in Fig. 2. The group delay response is periodic and the periodicity (dubbed as the free spectral range (FSR)) is inversely proportional to the round-trip time in the ring. Each period of the group delay response is a symmetric bell-shaped function of frequency, centered at the resonance frequency of the ring (Fig. 2). This resonance frequency can be varied by tuning the round-trip phase shift, ϕ, of the ring and the maximum delay can be tuned by varying the power coupling coefficient between the optical waveguide and the ring, κ. Here, the thermo-optical tuning mechanism is used to vary the resonance frequency and the coupling coefficient of the ORR. Two chromium heaters per ORR are used for the tuning, as illustrated in Fig. 2. The principle of this ORR as delay line can be found in detail in (Zhuang et al., 2007, 2010).

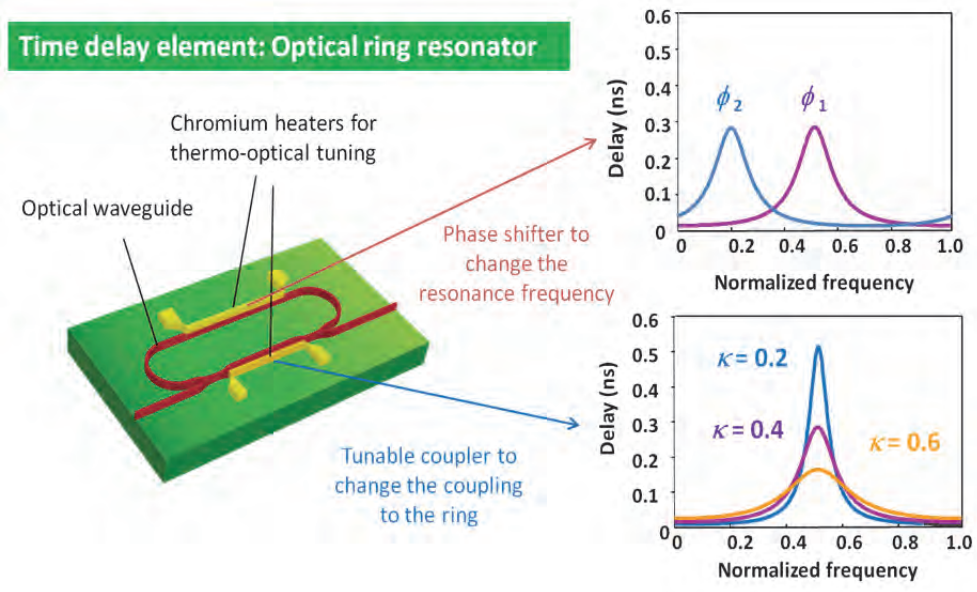

Fig. 2. Tunable optical delay based on an optical ring resonator. The group delay response of such an ORR is a bell-shaped function of the frequency, where its resonance frequency and maximum delay can be tuned using thermo-optical tuning mechanism.

The peak value of the delay is approximately inversely proportional to the width of curve since the area underneath the delay curve in one period is always constant. This imposes a trade-off between the highest delay values that can be provided while keeping the sufficient bandwidth. To overcome this, several ORRs can be cascaded, where the total group delay response is the sum of the individual ring responses. This is illustrated in Fig. 3.
In the next subsection, the principle of cascading the ORRs as tunable delay elements is used to yield the photonic BFN chip.

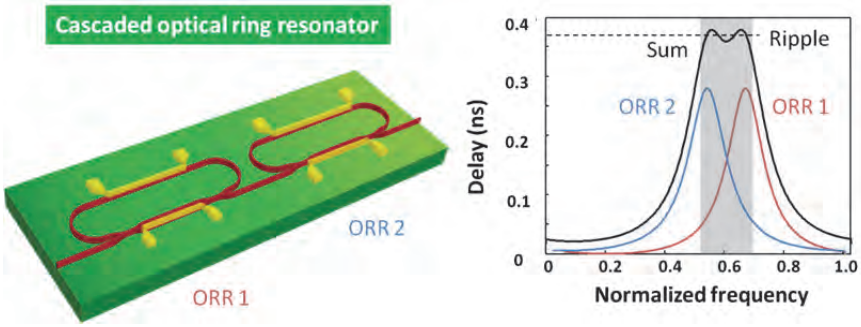

Fig. 3. Left: schematic of two serial ORRs, right: group delay response of a cascade of two ORRs is the sum of the group delay responses of the individual ORR. In this way, the maximum delay and the bandwidth of the response can be increased.

3.2 Optical beamforming chip

A full photonic BFN is obtained by combining the ORR based delay elements with power splitters and combiners. An example of a 16×1 photonic BFN is shown in Fig. 4. It is based on a binary tree topology, consisting of four sections, 16 inputs and one output (Meijerink et al., 2010). In this particular case a total of twenty rings are involved. The rationale for using such a topology is that, for a linear PAA, increasing delay tuning ranges are required for the sixteen possible paths through the photonic BFN. Based on the photonic BFN architecture presented here, sufficiently large delay over a wide bandwidth has been demonstrated. A delay as high as 1.2 ns (for a comparison, 1 ns is approximately 30 cm of propagation distance in vacuum) over a bandwidth of 2.5 GHz has been demonstrated with a cascade of 7 ORRs, in a 8x1 optical beamformer (Zhuang et al., 2007). The details of the photonic BFN design can be found in (Meijerink et al., 2010, Zhuang et al., 2010).

In the photonic BFN, the signal processing (i.e. delaying and combining) is done in the optical domain. For this reason, the received RF signals from the AEs need to be converted from the electrical domain to the optical domain. This is done using optical modulation in the optical modulators. As shown in Fig. 4, an array of 16 optical modulators interface with the 16x1 photonic BFN chip. The signal flow in this photonic BFN is shown in detail. The optical power from a continuous wave (CW) laser is injected to the input of the optical splitter chip (Fig. 4a). A tunable coupler is used to split the optical power into two paths: one path goes to a 1x16 splitter and then to the optical modulators (in this case, Mach-Zehnder modulators (MZMs)), while the other goes to an unmodulated path, which later on will be used for the carrier re-insertion. Meanwhile the received signal from the AEs are amplified with low noise amplifiers (LNAs) and supplied to the RF input of the MZMs (Fig. 4b). The MZMs are biased at the minimum transmission point, creating a double sideband-suppressed carrier modulated optical signals (Fig. 4c). Next, the ORRs in the photonic BFN are tuned to provide the desired delay to one of the signal sidebands (Fig. 4d). The unwanted sideband then is filtered using and optical sideband filter (OSBF) (Fig. 4e). This yield an optical single sideband suppressed carrier (OSSB-SC) signal. In order to restore the modulating RF signal, the OSSB-SC signal has to be combined with the re-inserted optical carrier in the carrier re-insertion coupler (Fig. 4f). The signal containing the desired sideband and the optical carrier is then detected using a balanced photodetector (BPD) (Fig. 4g). This detection scheme allows cancellation of common noise and distortion terms contained at the two outputs of the re-insertion coupler.

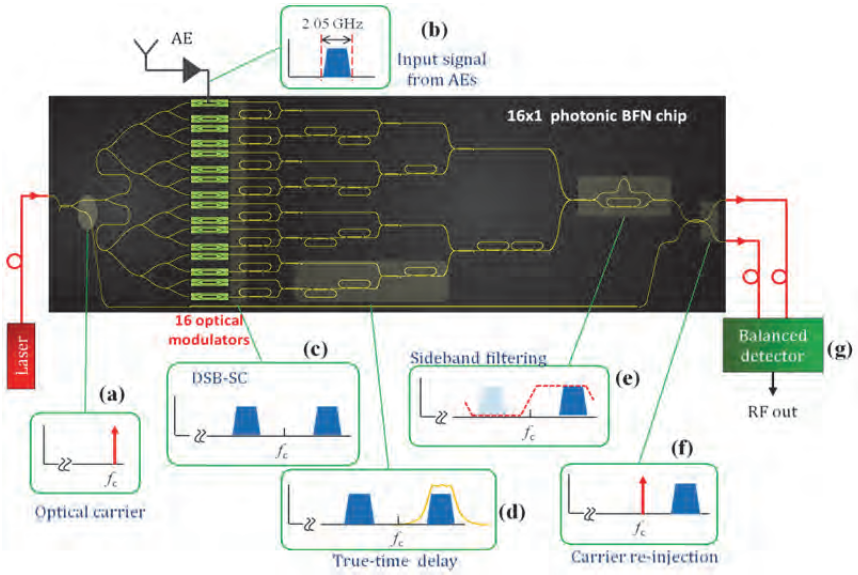

Fig. 4. Principle of operation of the photonic BFN system. The optical carrier from a laser (a) is modulated by the RF signals from the AEs (b) in the optical modulator array, yielding a DSB-SC spectrum (c). One of the sidebands of the optical signals are delayed and combined in the BFN (d) while the other is removed using an optical filter (e). The optical carrier is then recombined with the desired signal sideband (f) prior to the photodetection process in the balanced photodetector (g).

4. Phased array antenna system design

The photonic BFN explained in the previous section is the core of the total PAA system developed in this work. However, to beamform the signals from as many as 2048 AEs, one cannot use only a single photonic BFN. For this reason a scheme with two stages of optical beamforming is considered here (Marpaung et al., 2011, Meijerink et al., 2010). Two possibilities of how such a scheme can be implemented are illustrated in Fig. 5. In the first option (Fig. 5a), a tile consisting of 64 AEs is beamformed using a 64x1 photonic BFN. The (RF) outputs of thirty-two of these 64x1 photonic BFNs are then beamformed in the second stage using a 32x1 photonic BFN. This is the most straightforward implementation of the cascaded stages of photonic BFNs. However from previous investigations, it was concluded that a 64x1 photonic BFN presents a high degree of complexity and in turn imposes a higher risk in system reliability.

A way to avoid using very large photonic BFNs in the first stage is to combine RF beamforming and optical beamforming schemes as shown in Fig. 5b. In this scheme, every group of 4 AEs are combined using an RF beamforming scheme. Here, either (RF) time delay or phase shifting can be implemented. The latter will induce a beam squint but the effect is negligible since the required time delay between the neighboring AEs is relatively small (in the order of 34 ps). The use of RF beamforming will reduce the size of the photonic BFNs in the first stage to 16x1 instead of 64x1. These 16x1 photonic BFNs are well-investigated and relatively more reliable. Moreover, the scheme allows the use of an array of

16 modulators to interface with the photonic BFN instead of an array with 64 modulators which increases the yield of fabrication.

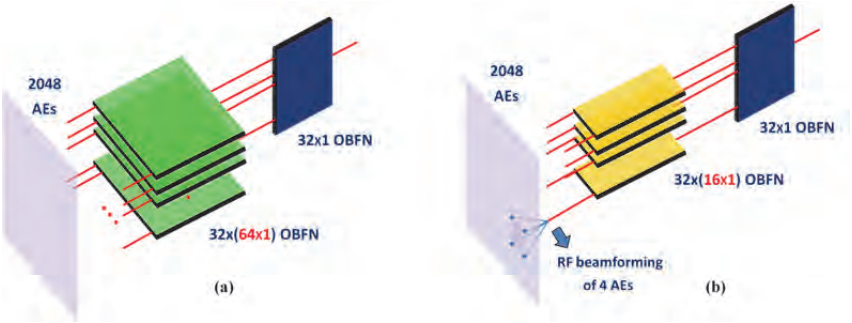

Fig. 5. Two options of implementing the two-stage optical beamforming scheme for a PAA with 2048 AEs. (a) In this scheme every 64 AEs in a tile is beamformed by a 64x1 photonic BFN. Outputs from 32 of these BFNs are combined in the second stage by a 32x1 photonic BFN. (b) A similar principle as in (a) but every group of 4 AEs is combined using RF beamformer. The first optical beamforming stage now consists of 32 of 16x1 photonic BFN.

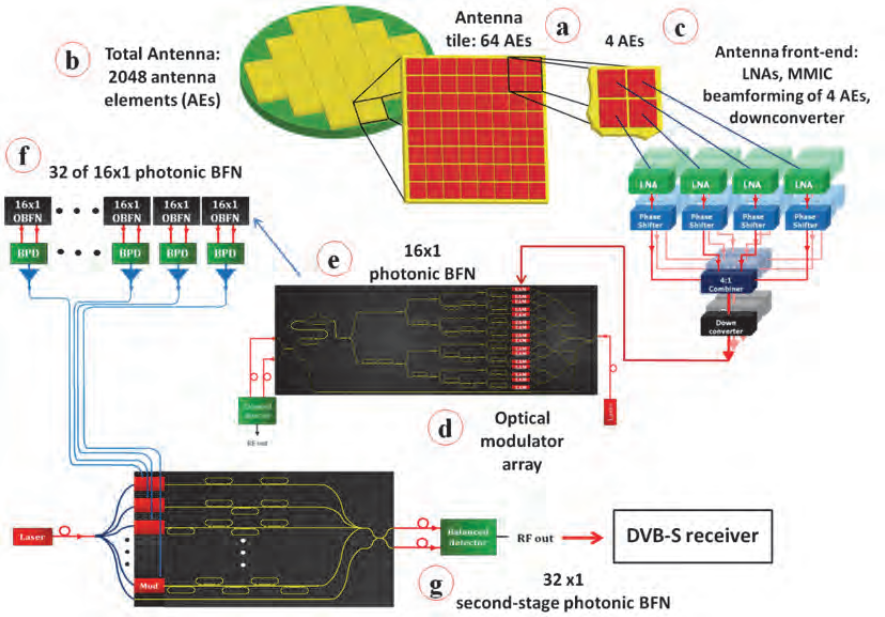

Fig. 6. The phased-array antenna system considered in this work. (a) An antenna tile consisting of 64 elements, (b) the total antenna system with >1800 AEs, (c) the RF front-end consisting of LNAs, MMIC phase shifter, a 4-to-1 combiner and a downconverter, (d) an array of optical modulator integrated with a 16x1 optical beamformer (e). The RF outputs of 32 of these 16x1 beamformer (f) are combined by a second stage optical beamfomer with 32 inputs and one output (g). BPD: balanced photodetector.

A more detailed schematic where the scheme in Fig. 5b is implemented is depicted in Fig. 6. The antenna tile (an 8x8 module) basic building block and the total antenna are shown in Figs. 6a and 6b, respectively. The antenna elements are stacked patch antennas that are impedance matched between 10.7 and 12.75 GHz (Verpoorte et al., 2011). In the antenna front-end, a chain of low noise amplifier (LNA) and monolithic microwave integrated circuit (MMIC) tunable phase shifter follows each AE. Using these phase shifters and a combiner, the RF beamforming is applied to a sub-array consisting of 4 neighbouring AEs. The output signal from the combiner is then down-converted to the L-band (Fig. 6c). The signals from the front end of each tile are then fed to an array of 16 optical modulators, to convert these signals to the optical domain (Fig. 6d). Each modulator array will interface with a 16x1 photonic BFN (Fig. 6e). Then, a larger photonic BFN with 32 input ports is used at the second-level to combine the outputs of 32 16x1 BFNs in the first stage (Fig. 6f and 6g). In the following section, the modelling and the performance evaluation of the entire system depicted in Fig. 6 is presented. The aim of this model is to retrieve the required system parameters of each component to meet the target specifications listed in Table 1.

4.1 System modeling

A procedure to simplify the complex PAA system depicted in Fig. 6 has been developed in order to analyze the system performance. The detail on the simplification procedure is beyond the scope of this chapter and has been reported elsewhere (Meijerink et al., 2010). The main idea is to reduce the dimension of such PAA system with multiple inputs and a single output into a two-port cascaded system. Eventually, to analyze such system the standard Friis' formula can be implemented (Meijerink et al., 2010). The resulting two-port model with its relevant parameters is depicted in Fig. 7. The system is now reduced to a cascade of an equivalent antenna and two blocks of receivers, each comprising an amplifier (the front end in the first block and the second-stage amplifier in the second block) and a two port model of the photonic BFNs (16x1 BFN in the first block and 32x1 BFN in the second block).

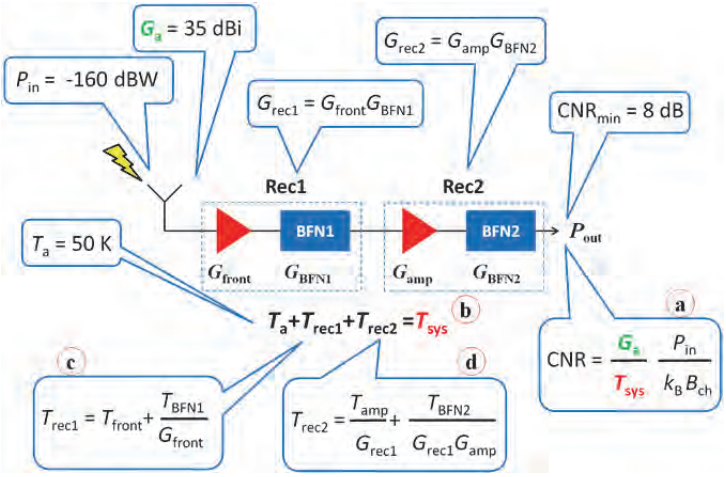

Fig. 7. Simplified two-port model of the PAA system in Fig.6.

For the system level simulation, some of the system parameters need to be fixed. From the antenna side, the gain and the antenna temperature are set to be 35 dBi and 50 K,

respectively. The antenna itself should receive signals from satellites, with a power level in the order of -150 dBW (assuming a satellite equivalent isotropic radiated power (EIRP) of 51 dBW) per transponder of 33 MHz bandwidth (Morello & Mignone, 2006). As will be shown later on, for some scenarios a margin up to 10 dB has been considered for this input power, leading to an input power as low as -160 dBW. The other parameters used in the simulation are listed in Table 2.

The model depicted in Fig. 7 shows the evolution of the gain and the noise temperature throughout the system. At the output, the system performance is evaluated in terms of the carrier to noise ratio (CNR) in the transponder bandwidth that should amount to at least 8 dB. This CNR is related to the G/T parameter mentioned in an earlier section by the equation (a) shown on Fig. 7. Using the values for the Boltzmann constant k_B=1.38×10^{-23} and B_{ch}=33×10^6 Hz, the CNR in dB and the G/T in dB/K is related by

$$\mathrm{CNR}(\mathrm{dB}) = G/T_{\mathrm{sys}}(\mathrm{dB/K}) + P_{\mathrm{in}}(\mathrm{dBW}) + 153.5. \quad (1)$$

As an example, to achieve an 8 dB minimum CNR with the antenna with G/T of 12.7 dB/K, as listed in Table 1, the minimum received power should amount to -158.2 dBW.

Having the model of the system established, the design objective now is to maximize the CNR in equation (a) of Fig. 7. To do so, the system noise temperature (T_{sys}) should be minimized, since in this study the other parameters (P_{in}, G_a and B_{ch} are fixed). As shown in equation (b) of Fig. 7, T_{sys} comprises the noise temperatures of the antenna (T_a) and the two equivalent receiver blocks (T_{rec1} and T_{rec2}). Again we consider a fixed value of T_a, thus dictating that T_{rec1} and T_{rec2} should be minimized.

Simulation parameter	Symbol	Value
Antenna noise temperature	T_a	50 K
Received signal power	P_{in}	Varied: -160 dBW to -150 dBW
Antenna gain	G_a	35 dBi
Transponder bandwidth	B_{ch}	33 MHz
Minimum output carrier-to-noise ratio in the transponder bandwidth	CNR_{min}	8 dB
Laser optical power	P_{laser}	100 mW
Laser relative intensity noise (RIN)	RIN	-150 dB/Hz
Balanced photodetector (BPD) responsivity	r_{PD}	0.8 A/W
BPD common mode rejection ratio	CMRR	30 dB
Load impedance	R_L	50 ohm
Second stage amplification gain	G_{amp}	30 dB
Second stage amplification noise figure	NF_{amp}	3 dB
Fiber-to-chip coupling loss	L_f	1 dB
Passband loss of the optical sideband filter	L_{OSBF}	1 dB
Front-end gain	G_{front}	Target: 70 dB
Front –end noise figure	NF_{front}	Target: 2.5 dB
Modulator half-wave voltage	V_π	Target: 4 V
Modulator insertion loss	L_m	Target: 5 dB
Optical waveguide propagation loss	L_{wg}	Target: 0.2 dB/cm

Table 2. System parameters used in the simulation and the performance analysis.

As shown in Friis' formulas in (c) and (d) of Fig. 7, these noise temperatures depend on the properties of the amplifiers and the BFNs. To minimize T_{rec1} one has to use a front-end with high gain and low noise figure (NF). Moreover, the noise temperature contribution of the first stage BFN (T_{BFN1}) should be kept low, such that at the end $T_{rec1} \approx T_{front}$. The BFN noise temperature itself is inversely proportional to the BFN gain (G_{BFN}) i.e.

$$T_{BFN} \propto \frac{1}{G_{BFN}}. \tag{2}$$

Thus, maximizing the gain of the BFN is paramount in achieving the required CNR. The BFN gain depends on the parameters of the optical components in the system, namely the laser, photodetector, the optical modulators and the photonic BFN chip. In this study we focus on the dependence of G_{BFN} to three key parameters, the optical waveguide propagation loss (L_{wg}) and the modulator half-wave voltage (V_π) and insertion loss (L_m). As shown in Eq. 3, G_{BFN} is inversely proportional to the square of the aforementioned parameters.

$$G_{BFN} \propto \frac{1}{\left(V_\pi \, L_m \, L_{wg}\right)^2} \tag{3}$$

Note that here the loss is defined in the range of [1, ∞] such that L=1 indicates a lossless system. Thus, it is important to limit the propagation loss in the optical waveguides as well as to ensure a highly efficient modulation in the modulators, characterized by low half-wave voltage and insertion loss. The optimum values of these parameters, together with the front-end gain and noise figure, will be determined from the system simulations in order to achieve the CNR_{min} specification. The other system parameters used in the simulation are also listed in Table 2.

4.2 System performance

In Fig. 8, the system CNR is shown as function of the optical waveguide loss in dB/cm at three different conditions. First, the front-end gain and the modulator V_π are set at 70 dB and 1 V, respectively. The rest of the parameters used are: P_{in}=-160 dBW, L_m=2 dB and NF_{front} = 0.7 dB. This, in fact, is describing the configuration with very high performance modulators and front-ends. With these parameters, the 8 dB CNR can be met for all waveguide loss values from 0 to 0.5 dB/cm (solid curve). But if the V_π increases to 4.0 V (which is more commonly found in commercial off-the shelf modulators), the specified CNR can only be met with L_{wg} of 0.2 dB/cm or lower (dashed-curve). If now the front-end gain is reduced to 60 dB, the CNR specification cannot be met with even with lossless optical waveguides (dash-dotted curve) (Marpaung et al., 2011). From these simulation results, the target value for G_{front} is set to 70 dB while the target value for the maximum L_{wg} is 0.2 dB/cm.

With a front-end gain of 70 dB and a low waveguide propagation loss the system noise temperature is likely to be dominated by the noise temperature of the front-end, T_{front} which is related to the front end noise figure (NF_{front}) via the relation:

$$NF_{front} = 10 \log_{10}\left(1 + \frac{T_{front}}{290}\right). \tag{4}$$

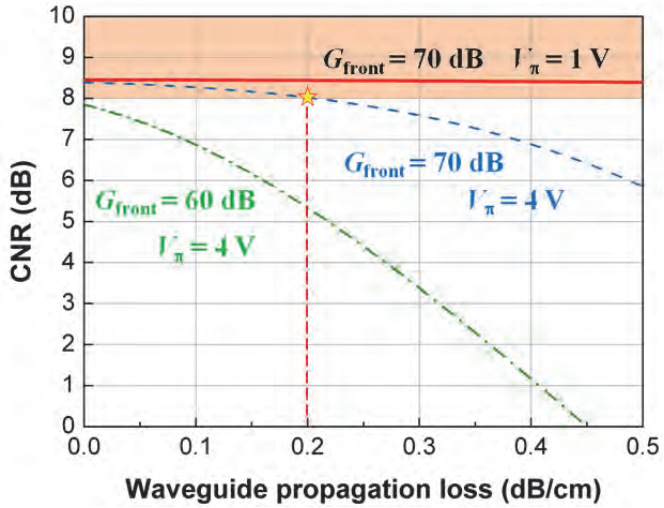

Fig. 8. Simulation results used to determine the requirements for G_{front} and L_{wg}. The system CNR is depicted as function of L_{wg} where G_{front} and V_π are used as parameters. The target L_{wg} value of 0.2 dB/cm is indicated by a star. The input signal power is -160 dBW.

In the simulation result presented in Fig. 8, it was assumed that T_{front} = 50 K what corresponds to NF_{front} = 0.7 dB. It could be challenging to achieve such a low value of NF. Thus, a simulation was carried out to determine the maximum front end NF that can be tolerated by the system to still achieve the target CNR. The result is depicted in Fig. 9.

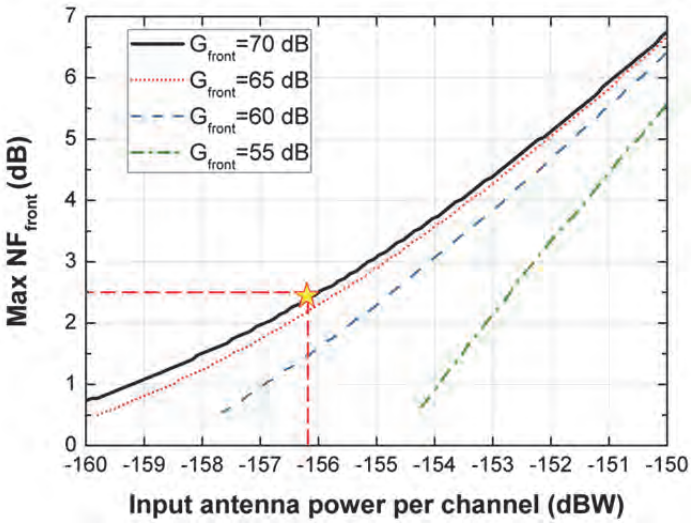

Fig. 9. Simulation results used to determine the maximum allowed NF_{front} as a function of the received signal power. The parameter values used are: V_π = 4 V, L_m = 2 dB and L_{wg} = 0.2 dB/cm. A target value of 2.5 dB front-end NF has been set, as indicated by a star symbol.

From the figure above one can determine that in order to achieve the required CNR with a received power of -160 dBW, the front end gain should be > 60 dB and NF < 1 dB. Since this is very challenging to achieve, the system requirement aimed in this work is slightly relaxed such that a power margin of 6 dB (input power of -156 dBW) is sufficient. Thus in this case, the NF requirement of the front-end is relaxed to < 2.5 dB for gain of 70 dB. These will be the target values for the front-end design.

Finally, to determine the parameters of the optical modulators, the simulation results in Fig. 10 are used. Here, the maximum allowed V_π to achieve 8 dB CNR is depicted as a function of the received RF power, with the modulator insertion loss is kept as a parameter. Although the front-end gain and NF are slightly different from the one determined in the previous simulation, the modulator parameters can still be determined. As mentioned earlier, to achieve the value L_m = 2 dB and low V_π simultaneously, one should employ a very high performance modulator. As suggested from the result in Fig. 10, to relax these requirements one should sacrifice a margin in the received power. Here, we have set preliminary target values of L_m = 5 dB and V_π = 4 V for the modulators, which allow a minimum received power of -154 dBW (i.e. a 4 dB power margin).

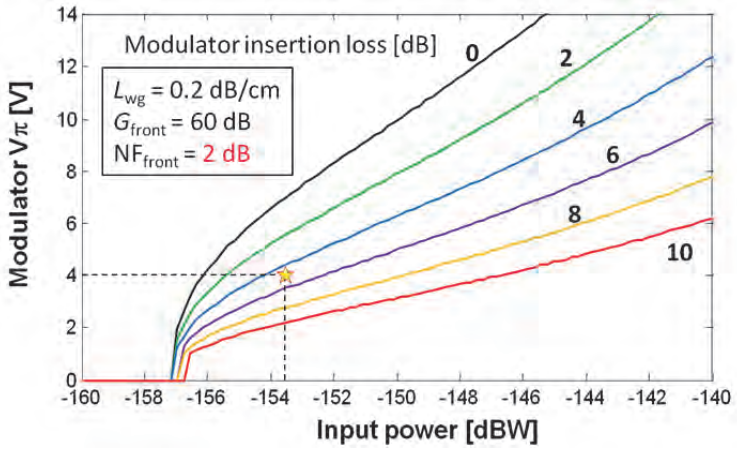

Fig. 10. Simulation results used to determine modulator parameters, V_π and L_m to achieve a minimum CNR of 8 dB. Preliminary target values of L_m = 5 dB and V_π = 4 V have been set, as indicated by a star symbol.

In the following section, the progress on the development of the components to achieve the target values determined earlier will be discussed.

5. Components development

From the system level simulation presented in the previous section the required characteristics of each component of the system have been specified. In the current phase of the SANDRA project numerous efforts have been directed towards meeting the specified performance. The development of three main parts that constitute an antenna tile (64 AEs), namely the front-ends (LNAs, phase shifters and downconverter chips), array of 16 optical modulators and the 16x1 photonic BFN chips are described in the following subsections.

5.1 Front-end

The projected configuration of the front-end is depicted in Fig. 11a. Here, the output signal of 4 AEs will be amplified, combined and subsequently downconverted to the L-band (950 3000 MHz). The target values of gain and noise figure for the complete chain have been set to 70 dB and 2.5 dB, respectively. From the front-end design point of view, downconversion to the L-band is advantageous to avoid oscillations due to the large amplification. The oscillations can be minimized by means of distributing the gain at the two frequency bands. Due to size constraints it is desirable to use MMICs with a high degree of integration. For this reason the so-called corechips will be used in the design. These are MMIC-building blocks that integrate different functionalities in the same chip. Here, the combined functionalities of amplification (LNA) and phase shifting are desired. The one selected for this design is a corechip that was previously designed for the NATALIA-project (Baggen et al., 2010) and manufactured by the foundry OMMIC. It consists of a two-stage LNA, 4 bit phase shifter and digital logic. The projected gain and NF of the corechip are 12 dB and 1.7 dB, respectively, with an assumption that the coupling loss from the antenna to the chip is less than 0.5 dB.

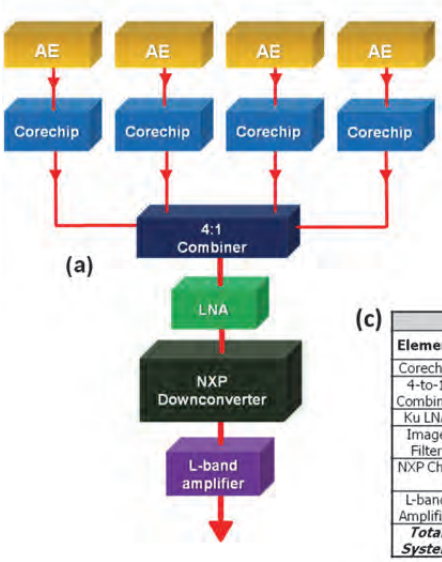

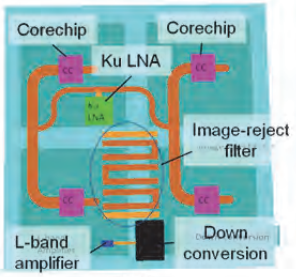

(c)

OVERVIEW OF GAIN AND NF			
Element	**Gain**	**NF**	**Components functionality**
Corechip	12	1.7	Amplification and Phase Shifting
4-to-1 Combiner	-1	1	Constructing a 2x2 Subgroup
Ku LNA	13	2	Second Stage Amplification
Image Filter	-3	2	Rejecting Image Frequencies
NXP Chip	35	9	Down-conversion and Amplification in Ku and L band
L-band Amplifier	14	4	Gain Compensation in L band
Total System	*70*	*2.4*	

Fig. 11. (a) The configuration of the front-end. The corechip consists of an LNA and a 4-bit phase shifter. The NXP chip is used for downconversion and amplification. (b) Schematic layout of the RF front-end. (c) Overview of the gain and noise figure of the elements of the front-end chain.

The outputs of the four corechips are subsequently combined in a 4:1 combiner followed by an LNA. The down-conversion is performed after combining the 2x2 sub array. The proposed chip for down-conversion here is manufactured by NXP. This chip is a highly integrated circuit that includes an LNA, a mixer, a down-converter, a phase-lock loop, a crystal oscillator, and an intermediate-frequency buffer. This chip supports RF input frequencies between 10.7 and 12.75 GHz, and uses a selectable LO that operates at 9.75 or

10.6 GHz. Finally an L-band amplifier is placed after the downconverter to achieve the gain in the L-band. The preliminary front-end layout of a 2x2 sub-array is depicted in Fig. 11b. The overview of the projected gain and noise figure of the complete front-end chain is summarized in Fig. 11c. A gain of 70 dB and a noise figure of 2.4 dB are achievable with this design which is in line with the target values set by the system simulations.

5.2 Optical modulator array

The electro-optic modulators developed in this work are surface-normal electroabsorption modulators (EAMs) based on InGaAs/InAlAs coupled quantum wells (Q. Wang et al., 2006). Compared to traditional waveguide EAMs, surface-normal EAMs offer significant advantages in terms of polarisation insensitivity, large active apertures and low insertion losses. A drawback of these modulators is the short interaction length between the incident light and the active medium, thus limiting the contrast ratio. Single-path surface-normal EAMs have typical contrast ratios in the range 2:1.

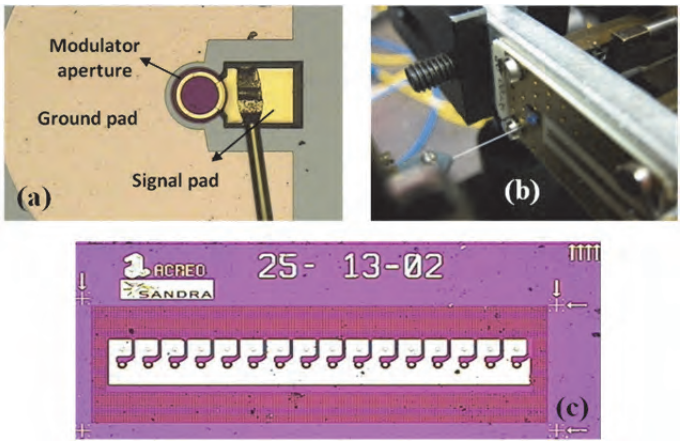

Fig. 12. (a) A microscope image of a surface normal electroabsorption modulator (EAM). (b) A photograph of the transmissive EAM mounted on a PCB. (c) A microscope image of a reflective EAM array consisting of 16 modulators. The pitch of the array is 127 μm and the chip size is 3.1 mm x 1.5 mm

The structure of a single modulator is shown in Fig. 12a, depicting a large area of ground pad, the modulator circular aperture and a pad to supply the reverse bias and the RF signal voltages. In this work, two types of EAMs with different diameters, ranging from 125 μm down to 25 μm, were fabricated. The first EAM type is the transmissive (i.e. single-path) modulator and the second type is the reflective (i.e. double-pass) modulator. The reflective EAM is obtained by means of depositing a mirror on one side of the modulator while the other side is anti-reflection coated. Thus, the incident light will experience twice absorption in the active area and the modulation contrast ratio will be enhanced but at the expense of an increased insertion loss. For test purposes, the modulator is mounted on a PCB using wire bonds. An SMA connector is then soldered to the PCB to supply the required reverse bias voltage and the RF signal. A photograph of a transmissive modulator on the PCB with optical fibers coupled at the input and output is shown in Fig. 12b. In Fig. 12c, the

photograph of an array of 16 reflective EAMs is depicted. The aperture size of these modulators is 25 μm. At the final system, this type of array will be interfaced with photonic the BFN chip by means of hybrid integration.

5.2.1 DC characterization

The characterization of the EAM started with the DC characteristics measurements. A tunable laser diode (TLD, Santec) is used to supply the light to the modulator and the output intensity is measured with an optical power meter (HP 8153A). Meanwhile the reverse bias voltage of the modulator is controlled using a variable power supply (HP 6634A). Various measurements were performed where all of them were automated in LabVIEW. First, the optical wavelength was swept from 1520 nm to 1580 nm with a step of 1 nm and the bias voltage was kept as a parameter and varied from 0 to 12 V with a step of 1 V. The optical power from the TLD was kept at 0 dBm. The transmission over the EAM as functions of the wavelength, with varying bias voltage, is shown in Fig. 13a. These results show that the EAM is more sensitive to bias voltage variations at two regions, roughly from 1530 nm to 1550 nm and at 1555 nm to 1570 nm. The modulator behaviours at these regions are different. In the lower wavelength region, an increase in the bias voltage results in a decrease in the transmission (or an increase in the absorption). In contrast, at the higher wavelength region, an increase in bias voltage results in an increase of transmitted optical power.

We also measured the transmission as a function of the bias voltage, for several optical wavelength values. This measurement is important to inspect the static linearity of the modulator transfer function (transmission vs. bias voltage). The results are shown in Fig. 13b, where a range from 1520 nm to 1545 nm is considered. We can see relatively linear responses are obtained in the bias voltage region of 2-8 V for a wavelength region of 1539 nm to 1541 nm. For λ = 1545 nm, the static characteristic is relatively linear up to 12 V of bias voltage. In the next parts, the RF characterization results of the modulators are reported.

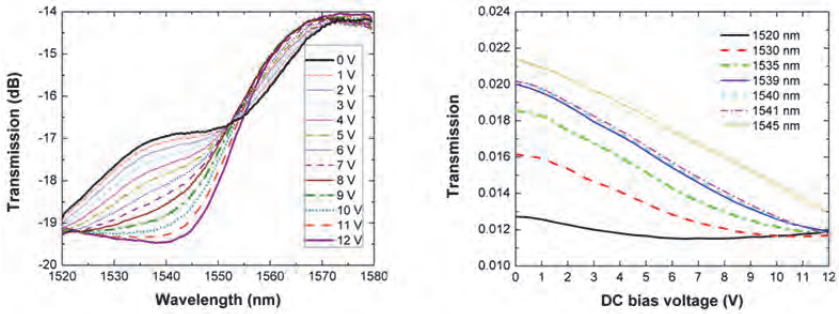

Fig. 13. DC characterisation results on a single pass (transmissive) EAM with an aperture of 100 μm. The input optical power to the modulator is set at 0 dBm. (a) The transmission through the modulator (in decibels) as a function of the optical wavelength for different reverse bias voltages. (b) Transmission (in linear scale) as a function of the reverse bias voltage, for various optical wavelengths from 1520 nm to 1545 nm

5.2.2 RF characterization: speed

The modulator speed depends on the size of the modulator. For a rough estimation of its bandwidth, the modulator can be modelled as an RC circuit where the capacitance depends linearly on the aperture area of the modulator. Thus, the smaller the modulator aperture, the higher cut-off frequency will be. For a relatively small EAM with an aperture diameter of 25 μm, the 3 dB cut-off frequency is expected to be in the order of 12 GHz. This is well above the intended frequency range of operation in the L-band (950-3000 MHz) resulting from the downconversion in the front-end.

To verify the modulator bandwidth, a measurement on the modulator frequency response (s_{21}) is carried out. Here the device under consideration is a reflective EAM with an aperture size of 25 μm. The measurement result for various reverse-bias voltages is depicted in Fig. 14a. Here, a laser with an optical wavelength of 1530 nm and an optical power of +9 dBm has been used as the optical source. It can be seen from the figure that in an extended frequency range of operation (1-5 GHz, marked as the shaded area in Fig. 14a) the modulator shows a relatively flat frequency response, with a 6-dB bandwidth of 5 GHz for a reverse bias of 3 V and 5 V (Marpaung et al., 2011).

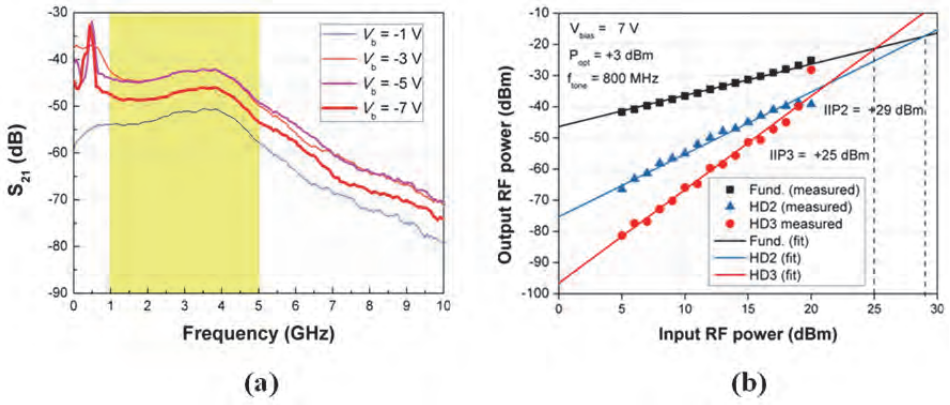

Fig. 14. RF characterization results on the EAMs. (a) The measured frequency response (s_{21}) of a reflective EAM with a 25 μm aperture for various reverse-bias voltages. The optical wavelength of the laser is 1530 nm. (b) The measured fundamental tone, HD2 and HD3 powers of a 100 μm aperture transmissive EAM for the bias voltage of 7 V at 1545 nm.

It is important to point out from Fig. 14a that the magnitude of the frequency response is relatively low (approximately -45 dB). The origin of this large RF-to-RF loss is still under investigation. Currently a lot of efforts are towards the improvement of the design and the quality of the wirebonds and the RF PCB used to mount the modulator. These improvements expectedly will lead to an accurate determination of the modulator V_π.

5.2.3 RF characterization: nonlinearity

Preliminary nonlinearity measurements have been performed on the transmissive EAM. For the particular EAM used in the experiments (100 μm aperture) the cut-off frequency is in the order of 1 GHz. A single-tone measurement was performed to probe the nonlinearities in the EAM. A modulating tone with a frequency of 800 MHz was supplied using an RF signal

generator. The EAM was reverse biased at 7 V while the optical wavelength was chosen at 1545 nm. The optical power from the TLD was set at +3 dBm. The RF tone power was then swept from +5 dBm up to +20 dBm with a step of 1 dB. The photodetector RF power was then measured with an RF spectrum analyzer at the fundamental, second-order harmonic (HD2) and third-order harmonic (HD3) distortions frequencies of 800 MHz, 1.6 GHz and 2.4 GHz, respectively. The measurement results are depicted in Fig. 14b. From these measurements, the 2nd-order and 3rd-order input intercept points (IIP2 and IIP3) of the EAM are determined to be +29 dBm and +25 dBm, respectively. As a comparison, for a Mach-Zehnder modulator with V_π = 4 V, the IIP3 is +21 dBm (Marpaung et al., 2010). Hence, the EAM under test under test have shown lower third-order nonlinearity relative to the aforementioned MZM. Currently, we are in the stage of extending these RF measurements to both types of modulators (transmissive and reflective) for various sizes.

5.3 16x1 photonic beamfomer chip

The photonic beamformer chip is developed using TriPleX waveguide technology (Bauters et al., 2011, Morichetti et al., 2007) that allows both low propagation loss and small bending radius to be achieved simultaneously. Three aspects regarding the 16x1 photonic BFN chip discussed here are the waveguide propagation loss, the layout of the photonic chip and the design of the optical sideband filter.

5.3.1 Waveguide propagation loss

As mentioned in the previous section, the target value for the maximum waveguide propagation loss is 0.2 dB/cm (at the optical wavelength range of 1530-1570 nm). Various test structures (for example directional couplers, spirals and ORRs) have been developed in the TriPleX technology with an optical waveguide structure consisting of a double stripe of which the cross-section is shown in the inset of Fig. 15.

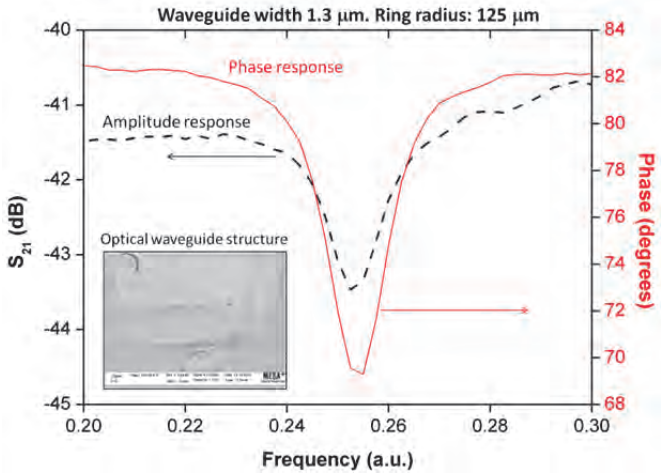

Fig. 15. Result of the propagation loss characterization of an optical ring resonator using the phase shift method. A loss of 0.2 dB/cm has been achieved. Inset: A scanning electron microscope (SEM) image of the waveguide cross-section.

A propagation loss measurement was performed in an ORR structure using the phase-shift method reported in (Roeloffzen et al., 2005). In this method, the ring resonators are tuned using a heater controller to its resonance frequency. The magnitude and the phase responses of this ring are then measured. The results are shown in Fig. 15. The measurement was performed on an ORR with a waveguide width of 1.3 μm and radius of 125 μm. This particular value was chosen to ensure that the measured loss is dominated by the waveguide propagation loss instead of the bend loss. From these measurements the propagation loss of the optical waveguide can be estimated to be as low as 0.2 dB/cm for TE polarized light which means that the target value from the system simulations has been met. Furthermore, from the simulation results it is expected that the bend loss will not become the dominant factor for a bending radius as low as 75 μm. It is important to mention that at these small bending radii a signifcant reduction of the optical beamformer chip can be realized as compared to previously developed BFNs (Marpaung et al., 2011).

5.3.2 Photonic chip layout

The 16x1 photonic BFN chip is designed to meet the criteria listed in Table 1. The layout of such a BFN follows the previous designs which use binary tree architecture. The important step in the design is to determine the optimum number of ORRs used in the chip. Due to the time-bandwidth product limitation explained in Section 3, the number of ORRs involved is estimated from the required maximum time delay and the signal bandwidth.

The maximum time delay in the BFN can be estimated from the information of the scanning angle, inter-element distance and how these elements are arranged in the tile. Fig. 16a shows the schematic of an 8x8 tile of 64 AEs. Here, d_{AE} is the distance between the antenna elements. Since an RF beamforming scheme is implemented in every group of 2x2 elements, the photonic BFN only "sees" the elements marked in (dark) red in Fig. 16a. The distance between the neighboring elements seen by the photonic BFN in this case is $d_{BFN}=2d_{AE}$. It can then be calculated that the maximum time delay between the elements seen by the 16x1 photonic BFN in this arrangement is

$$t_{max} = 3\sqrt{2}\ t_{BFN} = 6\sqrt{2}\ t_{AE} \tag{5}$$

The time delay needed between the adjacent elements (t_{AE}) is related to d_{AE} as follows

$$t_{AE} = \frac{d_{AE}\sin\theta}{c_0}. \tag{6}$$

Here θ is the maximum elevation scanning angle and c_0 is the speed of light in vacuum. Using the value of $\theta = 60^o$ and $d_{AE} = 1.18$ cm as listed in Table 1, one can calculate from Eqs. (5) and (6) that $t_{AE} = 34$ ps and subsequently $t_{max} = 290$ ps.

Although in this work the considered signal bandwidth is in the order of 2.05 GHz, the 16x1 photonic BFN is designed for larger bandwidth. The reason for this is to have the flexibility for the case that the antenna system needs to accommodate both the horizontal and vertical polarizations of the satellite signals in the future. Thus, in this case the minimum bandwidth for the BFN becomes 2x2.05 = 4.1 GHz. For this purpose the chip is designed to cover a bandwidth in excess of 4.3 GHz, which include a guard band.

It has been calculated that the time delay and bandwidth requirements derived earlier can be achieved with a BFN consisting of 40 ORRs. The resulting functional design and the

optical chip layout of the 16x1 BFN are shown in Fig. 16b and 16c, respectively. The BFN has been designed to be able to interface either with the transmissive or the reflective electroabsorption modulator arrays. A picture of the realized 16x1 BFN chip is depicted on Fig. 16d, together with a 20 cent Euro coin for size comparison. The total chip dimension of the BFN chip is 0.7 cm x 2.2 cm. This features a size reduction nearly 10 times compared to a 16x1 photonic BFN chip with a less complexity reported previously (Burla et al., 2010, Zhuang et al., 2010).

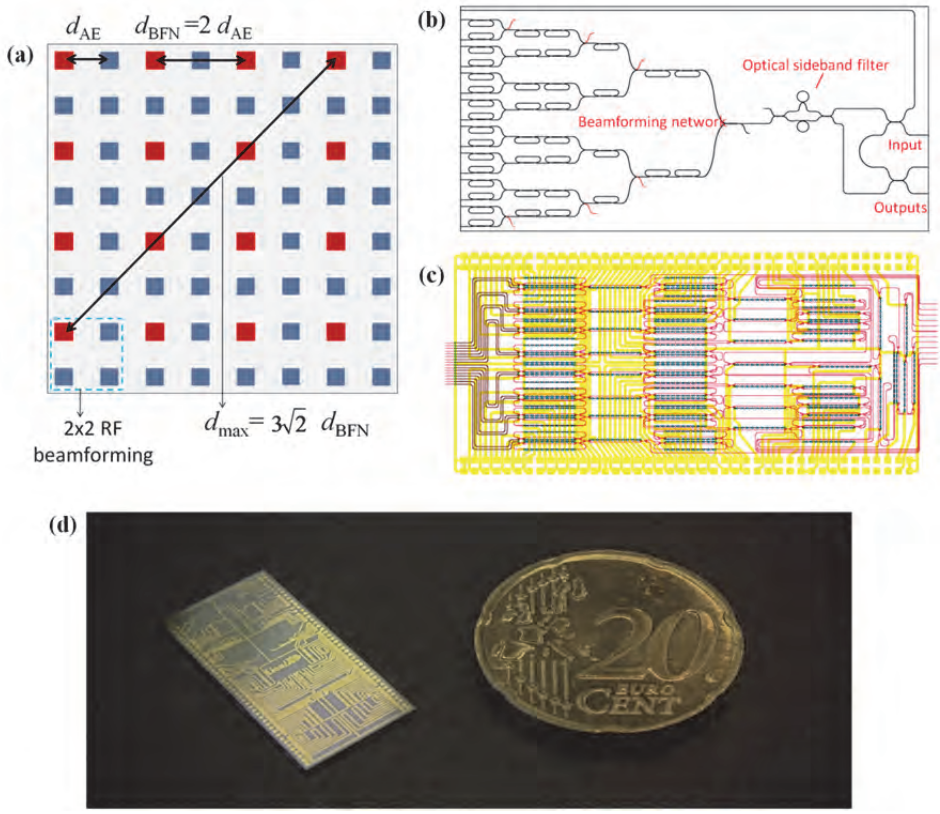

Fig. 16. (a) An antenna tile consisting of 64 AEs. (b) Functional design of the 16x1 photonic BFN showing the ORR delay elements and the sideband filter. (b) Chip layout of the BFN showing the optical waveguides, the heaters layout and the electrical wiring. The chip dimension is 0.7 cm x 2.2 cm. (d) The 16x1 photonic BFN chip pictured with a 20 cent Euro coin for size comparison.

5.3.3 Optical sideband filter

As mentioned earlier, the photonic BFN employs an OSSB-SC modulation scheme. In previous investigations (Meijerink et al., 2010, Zhuang et al., 2010), where MZMs instead of EAMs have been used, optical carrier suppression can be achieved by low-biasing the MZMs, while an optical filter is used to remove one of the signal sidebands. In that case a

Mach-Zehnder interferometer (MZI) with an ORR in one of its arms (MZI+1 ring) is used for the sideband filtering (Meijerink et al., 2010, Zhuang et al., 2010). In this work however, EA intensity modulators with a double-sideband with full carrier output spectrum are used instead of MZMs. Hence, an optical filter is required to suppress both the optical carrier and one of the sidebands. It turns out that an MZI+ 1 ring structure does not feature a transition that is sharp enough to do this. This is depicted in Fig. 17, where the measured and simulated responses of this filter are depicted, together with the position of the optical carrier. To improve the selectivity, an MZI structure where both arms are loaded with ORRs (MZI+2 rings) (Z. Wang et al., 2007) will be used for the filtering. The simulated response of such a filter is also depicted in Fig. 17, clearly depicting an improved selectivity and a narrower transition band. Both filters have been realized using the TriPleX waveguide technology. The waveguide layouts of these filters are depicted in Fig. 17. By means of fitting the measured response of the MZI+1 ring filter (Fig. 17), a waveguide propagation loss of 0.2 dB/cm is verified. The measurement on the MZI+2 rings filter is currently ongoing and will be reported elsewhere.

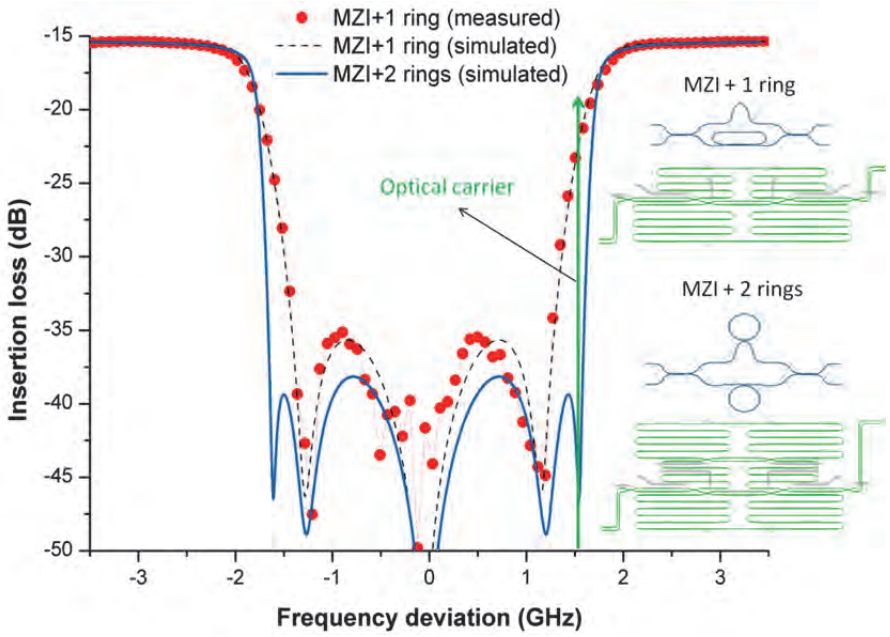

Fig. 17. Optical sideband filters measured and simulated responses. In the fitting a waveguide propagation loss of 0.2 dB/cm is used.

6. Photonic integration scheme

As mentioned in Subsection 3.2 the photonic BFN system employs optical single-sideband suppressed-carrier (OSSB-SC) modulation and coherent optical detection techniques. In this scheme to achieve proper combination of the signals optical phase synchronization of each branch of the BFN is required (Meijerink et al., 2010). To maintain the optical phase stability

in the photonic BFN chip itself has been shown to be viable (Zhuang et al., 2010). However, in the demonstration previously reported fiber pigtailed commercial off-the-shelf optical modulators have been used. This leads to a poor stability of the system. Thus, to depart from proof-of-concept towards an implementation in an actual PAA system, an important aspect that must be addressed is the photonic integration of the BFN chip and the optical modulator array.

A possible scheme for the integration of the 16x1 photonic BFN chip and the reflective EAM array is shown in Fig. 18. A carrier chip for the modulator array (fabricated using a silicon substrate covered by a thin SiO_2 film) is used to provide mechanical strength to the EAM chip as well as acting as the fan-out of the electrical paths going to the EAMs. The EAM chip is then flip-chip bonded onto the carrier chip. Before interfacing with the BFN chip the hybridization of the modulator chip is required. In this step the InP substrate of the EAMs has to be thinned down to reduce the insertion loss between the BFN chip and the modulator. It can be calculated that a substrate thickness of below 10 μm is required to achieve an insertion loss of below 3 dB between these two chips. The photonic BFN chip itself will be mounted on a PCB to provide the electrical paths to the heaters for thermo-optical tuning. The fiber-to-chip couplings of the laser and detector to the BFN chip will be done with butt-coupling. This photonic module will then be interfaced with the PCB containing the front-ends and the antenna tile using a connector array or a flex-cable.

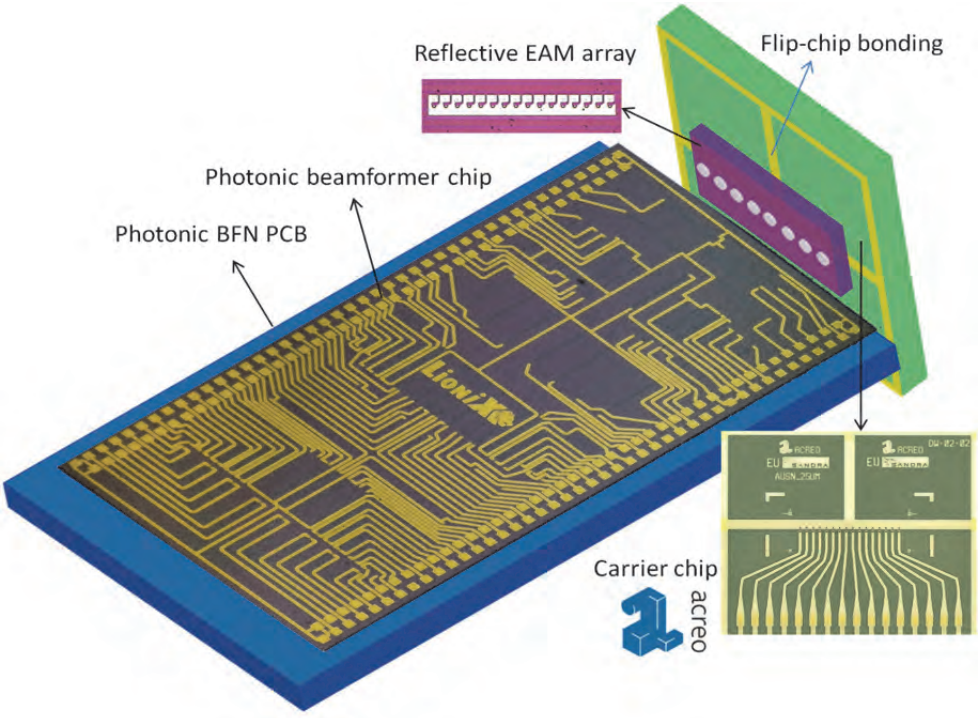

Fig. 18. An artist impression of a possible photonic integration scheme between the photonic BFN chip and the EAM array.

7. Conclusions

We have reported the design, performance analysis and the progress on components development of a novel Ku-band phased-array antenna system for airborne applications. A system level simulation has been used to determine the target values for the key parameters of the system components. Various target values like the front-end gain and noise figure as well as the propagation loss of the optical waveguide have been met. Development of two key components, namely the photonic BFN chip and the EAM array chip are reported. The first step towards the photonic integration of these chips is proposed.

8. Acknowledgment

The research leading to these results has been partially funded by the European Community's Seventh Framework Programme (FP7/2007-2013) under Grant Agreement n° 233679. The SANDRA project is a Large Scale Integrating Project for the FP7 Topic AAT.2008.4.4.2 (Integrated approach to network centric aircraft communications for global aircraft operations). The project has 31 partners and started on 1st October 2009.
The authors would like to thank L. Zhuang, M. Burla, A. Meijerink, A. Leinse, Q. Wang, D. Platts, A. Hulzinga, P. Jorna, H. Schippers, B. Sanadgol and M. Campo for their contributions to this work.

9. References

Baggen, R.; Vaccaro, S.; del Rio, D. ; Sanchez, R. & Langgartner, G. (2010). First Prototyping of a Compact Mobile K_u-band Satellite Terminal. *Proceedings of the 4th European Conference on Antennas and Propagation (EuCAP 2010),* pp. 1-5, ISBN 978-84-7653-472-4, Barcelona, Spain, April 2010

Baggen, R.; Holzwarth, S.; Böttcher, M. & Sanadgol, B. (2011). Phased Array Technology for Mobile User Terminals. *Proceedings of the 5th European Conference on Antennas and Propagation (EuCAP 2011),* pp. 2782-2786, ISBN 978-88-8202-074-3, Rome, Italy, April 2011

Bauters, J.; Heck, M.; John, D.; Dai, D.; Tien, M.; Barton, J.; Leinse, A. ; Heideman, R.; Blumenthal, D. & Bowers, J. (2011). Ultra-Low-Loss High-Aspect-Ratio Si_3N_4 Waveguides. *Optics Express,* Vol. 19, No. 4, February 2011, pp. 3163-3174, ISSN 1094-4087

Burla, M.; Khan, M.R.H.; Marpaung, D.; Roeloffzen, C.; Maat, P.; Dijkstra, K.; Leinse, A.; Hoekman, M. & Heideman, R. (2010). Squint-free Beamsteering Demonstration using a Photonic Integrated Beamformer based on Optical Ring Resonators. *Proceedings of the IEEE Topical Meeting on Microwave Photonics (MWP 2010),* pp. 1-4, ISBN 978-1-4244-7824-8, Montreal, Canada, October 2010

Marpaung, D.; Roeloffzen, C.; Leinse, A. & Hoekman, M. (2010). A Photonic Chip based Frequency Discriminator for a High Performance Microwave Photonic Link. *Optics Express,* Vol. 18, No. 26, December 2010, pp. 27359-27370, ISSN 1094-4087

Marpaung, D.; Zhuang, L.; Burla, M.; Roeloffzen, C.; Verpoorte, J.; Schippers, H.; Hulzinga, A.; Jorna, P.; Beeker, W.P.; Leinse, A.; Heideman, R.; Noharet, B.; Wang, Q.; Sanadgol, B. & Baggen, R. (2011). Towards a Broadband and Squint-free K_u-band Phased Array Antenna System for Airborne Satellite Communications. *Proceedings of the 5th European Conference on Antennas and Propagation (EuCAP 2011),* pp. 2774-2778, ISBN 978-88-8202-074-3, Rome, Italy, April 2011

Meijerink, A.; Roeloffzen, C.; Meijerink, R.; Zhuang, L.; Marpaung, D.; Bentum, M. ; Burla, M. ; Verpoorte, J. ; Jorna, P. ; Hulzinga, A. & van Etten, W. (2010). Novel Ring Resonator-Based Integrated Photonic Beamformer for Broadband Phased Array Receive Antennas—Part I: Design and Performance Analysis. *Journal of Lightwave Technology,* Vol. 28, No. 1, January 2010, pp. 3-18, ISSN 0733-8724

Morello, A. & Mignone, V. (2006). DVB-S2 : The Second Generation Standard for Satellite Broad-Band Services. *Proceedings of the IEEE*, Vol. 94, No. 1, January 2006, pp. 210-227, ISSN 0018-9219

Morichetti, F.; Melloni, A. ; Martinelli, M.; Heideman, R.; Leinse, A.; Geuzebroek, D. & Borreman, A. (2007). Box-Shaped Dielectric Waveguides : A New Concept in Integrated Optics. *Journal of Lightwave Technology,* Vol. 25, No. 9, September 2007, pp. 2579-2589, ISSN 0733-8724

Riza, N.A & Thompson, J.B. (Eds.). (1997). *Selected Papers on Photonic Control Systems for Phased Array Antennas, Series SPIE Milestone Vol. MS136,* SPIE Press, ISBN 9780819426130, New York

Roeloffzen, C.; Zhuang, L.; Heideman, R.; Borreman A. & van Etten, W. (2005). Ring Resonator-Based Tunable Optical Delay Line in LPCVD Waveguide Technology. *Proceedings IEEE/LEOS Benelux Chapter 2005*, pp. 79-82, Mons, Belgium, December 2005

SANDRA project website, May 2011, Available from : www.sandra.aero

Verpoorte, J.; Schippers, H.; Jorna, P.; Hulzinga, A.; Roeloffzen, C.; Marpaung, D.; Sanadgol, B.; Baggen, R.; Wang, Q.; Noharet, B. ; Beeker, W.; Leinse, A. & Heideman, R. (2011). Development of the SANDRA Antenna for Airborne Satellite Communication. *Proceedings of the IEEE Aerospace Conference 2011,* pp. 1-15, ISBN 978-1-4244-7350-2, Big Sky, MT, March 2011

Wang, Q.; Noharet, B.; Junique, S. ; Agren, D. & Andersson, J. (2006). 1550 nm Transmissive/Reflective Surface-Normal Electroabsorption Modulator Arrays. *Electronics Letters*, Vol. 42, No. 1, January 2006, pp. 47-49, ISSN 0013-5194

Wang, Z.; Chang, S.; Ni, C. & Chen, Y. (2007). A High-Performance Ultracompact Optical Interleaver Based on Double-Ring Assisted Mach–Zehnder Interferometer. *IEEE Photonics Technology Letters,* Vol. 19, No. 14, July 2007, pp. 1072-1074, ISSN 1041-1135

Zhuang, L.; Roeloffzen, C.; Heideman R. ; Borreman A. ; Meijerink, A. & van Etten, W. (2007). Single-chip Ring Resonator-based 1x8 Optical Beamforming Network in CMOS-compatible Waveguide Technology. *IEEE Photonics Technology Letters,* Vol. 19, No. 13, July 2007, pp. 1130-1132, ISSN 1041-1135

Zhuang, L.; Roeloffzen, C.; Meijerink, A.; Burla, M.; Marpaung, D.; Leinse, A.; Hoekman, M.; Heideman, R. & van Etten, W. (2010). Novel Ring Resonator-Based Integrated Photonic Beamformer for Broadband Phased Array Receive Antennas—Part II: Experimental Prototype. *Journal of Lightwave Technology,* Vol. 28, No. 1, January 2010, pp. 19-31, ISSN 0733-8724